CrossMark

Studies on Electrical and Magnetic Properties of Mg-Substituted Nickel Ferrites

PRADEEP CHAVAN,[1] L.R. NAIK,[1,6] P.B. BELAVI,[2] GEETA CHAVAN,[3] C.K. RAMESHA,[4] and R.K. KOTNALA[5]

1.—Department of Studies in Physics, Karnatak University, Dharwad, Karnataka 580 003, India. 2.—Department of Physics, Gogte Institute of Technology, Belagavi, Karnataka 590 008, India. 3.—Department of Physics, Karnataka Science College, Dharwad, Karnataka 580 003, India. 4.—BITS Pilani, K. K. Birla Goa Campus Zuarinagar, Sancoale, Goa 403726, India. 5.—National Physical Laboratory, K. S. Krishnan Marg, Pusa, New Delhi 110012, India. 6.—e-mail: naik_40@rediffmail.com

The semiconducting polycrystalline ferrite materials with the general formula $Ni_{1-x}Mg_xFe_2O_4$ were synthesized by using the solid state reaction method. X-ray diffraction (XRD), Fourier transform infrared (FTIR) spectrographs, and atomic force microscopy techniques were utilized to study the structural parameters. XRD confirms the formation of single phase cubic spinel structure of the ferrites. The crystallite sizes of ferrites determined using the Debye–Scherer formula ranges from 0.963 μm to 1.069 μm. The cation distribution of ferrite shows that Mg^{2+} ions occupy a tetrahedral site (A-site) and the Ni^{2+} ion occupy an octahedral site (B-site) whereas Fe^{3+} ions occupies an octahedral as well as a tetrahedral site. The study of elastic parameters such as the longitudinal modulus, rigidity modulus, Young's modulus, bulk modulus, and Debye temperature were estimated using the FTIR technique. The decrease of direct current (DC) resistivity with increase in temperature indicates the semiconducting nature of ferrites. The dielectric constant as well as loss tangent decreases with increase in frequency, and at still higher frequencies, they are almost constant. This shows usual dielectric dispersion behavior attributed to the Maxwell–Wagner type of interfacial polarization and is in accordance with Koop's phenomenological theory. The linear increase of alternating current conductivity with increase of frequency shows the small polaron hopping type of conduction mechanism in all the ferrites. The magnetic properties such as saturation magnetization (M_s), magnetic moment, coercivity, remnant magnetization (M_r), and the ratio of M_r/M_s was estimated using the M–H loop.

Key words: Powder x-ray diffraction (XRD), atomic force microscopy (AFM), Fourier transform infrared (FTIR) spectrograph, electrical resistivity, Debye temperature, Tauc plot, vibrating sample magnetometer (VSM) and magnetic moment

INTRODUCTION

Cubic spinel structured ferrites have potential applications in the field of magnetic and electronic technology; they also have a wide range of applications in drug delivery systems and in medical diagnosis.[1] Ferrites having high electrical resistivities, high saturation magnetization, and low dielectric losses are useful in microwave devices, computer memories, and magnetic recording devices. Ferrites are good magnetic material with more stability; thus they are used in transformer cores, high quality filters, radio wave circuits ,and

operating devices, etc.[2] These materials are low cost and can easily be prepared; they show high electrical resistivity and are widely applicable for the cores of intermediate and high frequency electromagnetic devices. The magnetization is an important property of magnetic materials to decide their applications in various fields such as electronic devices, electric motors, and permanent magnets, etc., depending on various aspects of the hysteresis loop. The electrical and dielectric properties provide necessary information about the behavior of electron charge carriers that lead to a good understanding and explanation of the conduction mechanism of electrons in ferrites. AC conductivity is one of the important properties of ferrites at high frequency applications. The electrical conductivity and dielectric behavior of ferrites depend on the sintering time, temperature, composition, and preparation conditions as well as the quantity and type of additives. It seems that addition of small rare earth metals play an important role in modifying the structure and magnetic properties of ferrites due to the magnetocrystalline anisotropy in rare earth-substituted compounds. Ferrites exhibit super magnetic properties such as high saturation magnetization and lower coercivity as compared to polycrystalline materials. Due to the important applications, electrical conductivity and dielectric properties of Ni–Mg ferrites[3,9] and Ni–Zn ferrites were studied by earlier researchers.[4–8] Thus, the choice of ferrites for a particular application depends on its electrical and magnetic properties. $NiFe_2O_4$ is one of the most important materials with an inverse spinel structure and is a well-known magnetic material.

Magnesium is a paramagnetic material with low weight, good electrical and mechanical properties, and was used in manufacturing mobile phones, laptops, storage devices, etc. Magnesium is readily available and relatively nontoxic, therefore Mg is used as a dopant. In the present paper, we have studied how the substitution of the Mg ion (for different concentrations) affects the crystallite size, lattice constant, porosity, binding nature of materials, conduction mechanism, Curie temperature, activation energy, variation of drift mobility as a function of temperature, dielectric relaxation, band gap energy, magnetic moment, saturation magnetization, and remnant magnetization for $Ni_{1-x}Mg_xFe_2O_4$ ferrites.

EXPERIMENTAL DETAILS

Polycrystalline ferrites having the chemical composition $Ni_{1-x}Mg_xFe_2O_4$, in which x varies from 0.0 to 0.5, were synthesized by the solid state reaction method. The high purity analytical reagent grade metal oxides of fine grain powders NiO, MgO, and Fe_2O_3 were used as the starting material for the preparation. These metal oxides are weighed in the required molar proportion according to the stoichiometry. The weighed metal oxides are ground in acetone medium continuously for about 4–5 h in a planetary agate mortar to obtain the homogenous mixture of oxides. The long duration of grinding also helps in decreasing the grain size. The mixture is presintered at 800°C for 8 h in a muffle furnace in air medium and cooled to room temperature. The fine grounded powder is mixed with polyvinyl alcohol (2% solution), which acts as a binding agent, and it is further pressed into pellet form of 10 mm diameter and 2–3 mm thickness by applying a pressure of 7 tons/cm^2 for 5 min using a hydraulic KBr press. These pellets were kept in a programmable furnace for final sintering at 1150°C for 12 h.

CHARACTERIZATIONS

The structural formation of ferrites was confirmed by the x-ray diffractometer (Model: Rigaku Miniflex) with Cu–Kα X-radiation ($\lambda = 1.5406$ Å). The absorption bands are analyzed using FTIR Spectrograph (Model: Nicolet–Impact, 410, America). The surface morphology and grain size are estimated using AFM (Model: Nanosurf Easyscan2). DC resistivity is carried out by using the two-probe technique. The dielectric properties of ferrites are measured with frequency ranging from 20 Hz to 1 MHz at room temperature using inductance, capacitance, and resistance (LCR) meter bridges (Model: N4L PSM1700). The absorption spectra of ferrites are characterized by using an ultraviolet–visible (UV–Vis) Spectrophotometer (Model: V-670, JASCO International). The saturation magnetization and magnetic moment are estimated with the help of a vibrating sample magnetometer (VSM) (Model: VSM 735 Lakeshore, NPL New Delhi).

RESULTS AND DISCUSSION

XRD Analysis

The XRD pattern of the single phase cubic spinel structure of ferrites is as shown in Fig. 1. All peaks in the XRD pattern are identified and indexed with the help of 'American Society for Testing and Materials' (ASTM) data, which confirms the formation of single phase cubic spinel structure without any impurities in all samples.[10] The prominent peak (3 1 1) observed in all the ferrite samples confirms the existence of the single phase cubic spinel structure of ferrite. The crystallite sizes of ferrites were estimated from the broadening of high intense diffraction peaks, i.e., (3 1 1) by using the Debye–Scherer equation as follows,

$$\delta = \frac{K\lambda}{\beta \cos \theta} \tag{1}$$

where K is the constant (i.e., $K = 0.9$), λ is the wavelength of x-ray, β is the full width half maximum (FWHM), and θ is Bragg's angle.

The estimated values of crystallite size, lattice constant, and porosity of the ferrites are tabulated in Table I. It is observed that the crystallite size of ferrites increases with increase of Mg concentration. The crystallite sizes of ferrites ranges from 0.963 μm to 1.069 μm. From the Table I, it is observed that the lattice constant increases with increase of Mg^{2+} ion content in ferrites; this is due to the difference in ionic radii of the component ions in the ferrite systems. The ionic radii of Mg^{2+} ions (0.072 nm) are slightly greater than Ni^{2+} (0.069 nm) and Fe^{3+} ions (0.0645 nm),[11] this gives evidence for the variation of lattice constant with increasing Mg^{2+} ions in the ferrite system. The porosity of ferrites were estimated by using the relation as follows,

$$\%Porosity = \frac{(d_x - d_a)}{d_x} \times 100 \qquad (1a)$$

where d_x = x-ray density, d_a = actual density.

Porosity is the inherent phase in ceramics prepared by sintering and powder processing. A high rate of sintering with small crystallite size reduces the porosity appreciably. The porosity of ferrites increases with increase of Mg^{2+} ion content in the ferrites. The estimated values are in the range from 10.8% to 24.9% (Table I).

FTIR Studies

FTIR spectra of ferrites with different concentrations of Mg are shown in Fig. 2. Particularly in single phase cubic spinel ferrites, two prominent absorption bands are observed (Table I). The strongest band appeared around 609 cm^{-1} and corresponds to intrinsic stretching vibrations of the metal ions in the tetrahedral site, whereas the weak band observed around 422 cm^{-1} is assigned to M–O stretching in the octahedral site. The metal–oxygen bonds vibration at the octahedral site and the difference in Fe^{3+}–O^{2-} distances at tetrahedral sites,[12–14] gives rise to the absorption bands in the single phase cubic spinel crystal lattice. In ferrite materials, the metal ions are situated in two different sublattices, namely, tetrahedral site (A-site) and the octahedral site (B-site).[15,16] The
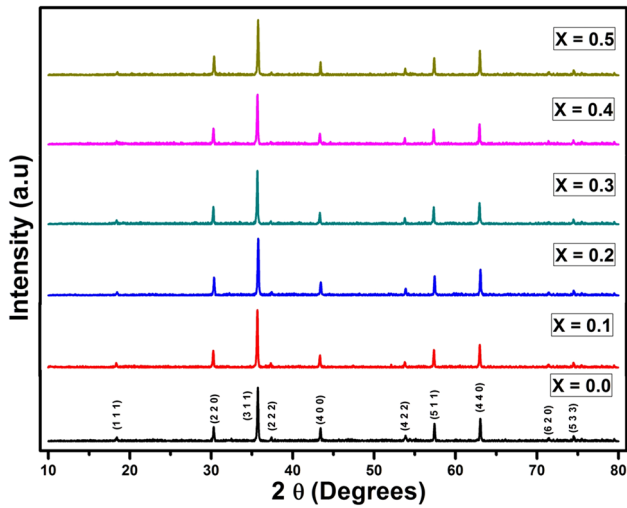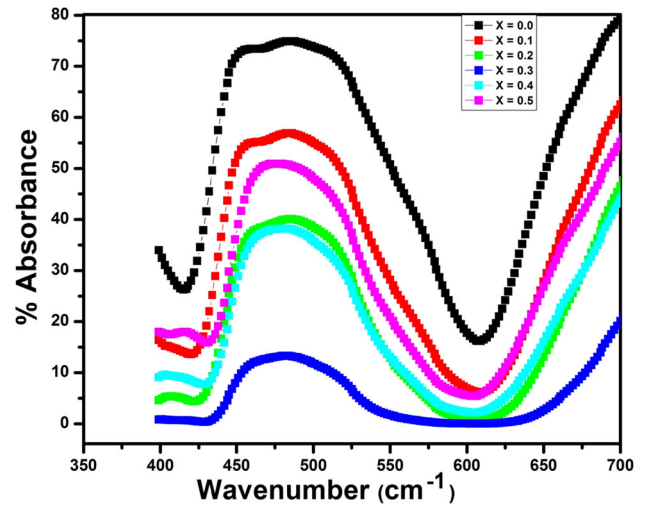

Fig. 1. XRD graphs of $Ni_{1-x}Mg_xFe_2O_4$ ferrites.

Fig. 2. IR absorption bands of $Ni_{1-x}Mg_xFe_2O_4$ ferrites.

Table I. The crystallite size, lattice constant, absorption bands, porosity, and activation energy of paramagnetic (ΔE_1) and ferromagnetic (ΔE_2) regions and band gaps

X composition	crystallite size (μm)	Lattice constant (a)	IR absorption bands		Porosity (%)	Activation energy (eV)		Optical band gap (eV)
			v_1 (cm^{-1})	v_2 (cm^{-1})		ΔE_1	ΔE_2	
0.0	0.963	8.3306	415	604	10.8	1.33	0.783	3.04
0.1	1.043	8.3353	420	607	18.4	1.65	0.762	2.83
0.2	1.050	8.3440	422	609	19.1	1.46	0.716	2.95
0.3	1.069	8.3471	424	609	21.5	1.50	0.823	3.01
0.4	1.064	8.3472	426	609	24.2	2.85	0.849	2.93
0.5	1.069	8.3476	427	608	24.9	2.96	0.854	3.04

absorption band (v_1) was caused by the stretching vibrations of the tetrahedral metal oxygen band and the absorption band (v_2) was caused by the metal oxygen vibrations in the octahedral site. The cation distribution of ferrites was estimated by using the following relation,

$$[Mg_xFe_{1-x}]^A[Ni_{1-x}Fe_{1+x}]^BO_4^2 \qquad (2)$$

The cation distribution of ferrite shows that the Mg^{2+} ion occupies the tetrahedral site (A-site) and the Ni^{2+} ion occupies the octahedral site (B-site); whereas Fe^{3+} ions occupy the octahedral as well as the tetrahedral site. Substitution of Mg^{2+} ions in the system decreases the amount of Ni^{2+} and increases the amount of Fe^{3+} ions in the octahedral B-site and shifts the band position (422 cm^{-1}) towards the lower wavelength. The displacement of Fe^{3+} ions in the B-site by the smaller Mg^{2+} ions will result in a somewhat decrease in the metal–oxygen bond length and, consequently, increase the wave number of the v_2 band.[10,11]

AFM Studies

The surface morphology of ferrite samples was measured using noncontact mode (dynamic mode) by AFM technique and is shown in Fig. 3. We observed that the synthesized samples shows the spherical shape with an average grain size of about 751 nm, with occurrence of agglomeration to some extent. The grain sizes of ferrites are completely dependent on the chemical composition, the preparation conditions, the cell volume, the secondary phases, and the agglomeration behaviour of grains.

From Fig. 3, it is observed that the average grain size of ferrite samples with $x = 0.5$ is found to be around 1.51 μm, which is the largest among the five samples because of the replacement of a limited amount of Mg^{2+} ions from Fe^{3+} ions, thus at $x = 0.5$ the expansion of the spinel lattice reaches its maximum.[17] The average grain sizes of the ferrites estimated from the AFM technique are in good agreement with the grain sizes determined from XRD using the Debye–Scherer formula.

Electrical Properties

Temperature Dependent DC-Resistivity

The variation of DC resistivity as a function of temperature is as shown in Fig. 4. From the Figure, we notice that the DC resistivity for all ferrite samples decreases with increase in temperature, indicating the semiconducting nature of ferrites. This may be attributed to the increase in drift mobility of the charge carriers and which mainly depends on density, porosity, grain size, chemical composition, etc.[18] Further, the conduction mechanism of electrons in all ferrites may be due to the hopping of electrons from Fe^{2+} to Fe^{3+} ions. The exchange of electrons between $Fe^{2+} \leftrightarrow Fe^{3+} + e^-$ is responsible for n-type charge carrier, and the exchange of holes between $Ni^{3+} \leftrightarrow Ni^{2+} + e^+$ and $Mg^{2+} \leftrightarrow Mg^{1+} + e^+$ is responsible for p-type charge carriers in the ferrite phase. The numbers of such ion pairs depend upon the sintering conditions and the amount of reduction of ions from Fe^{2+} to Fe^{3+} at certain temperatures.[18] The conduction mechanism of ferrites explained on the basis of the Verwey and De-Boer mechanism,[19] which involves the exchange
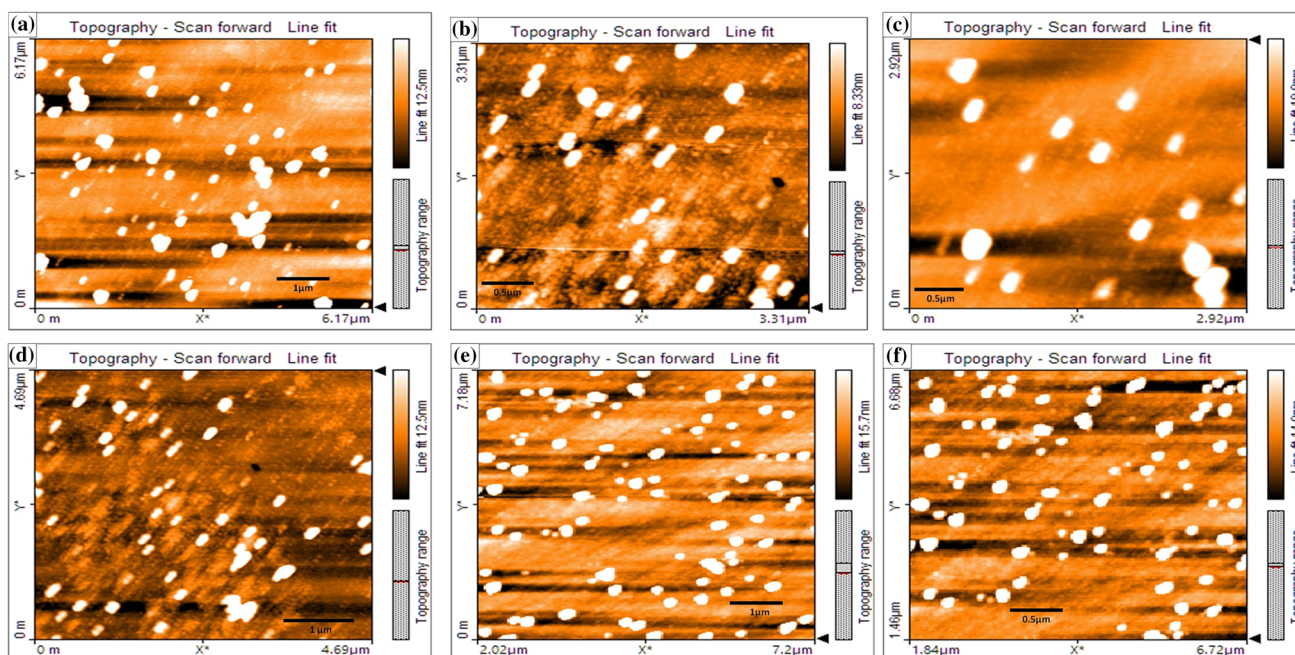

Fig. 3. AFM images of $Ni_{1-x}Mg_xFe_2O_4$ ferrites [where (a) = 0.0, (b) = 0.1, (c) = 0.2, (d) = 0.3, (e) = 0.4, and (f) = 0.5].

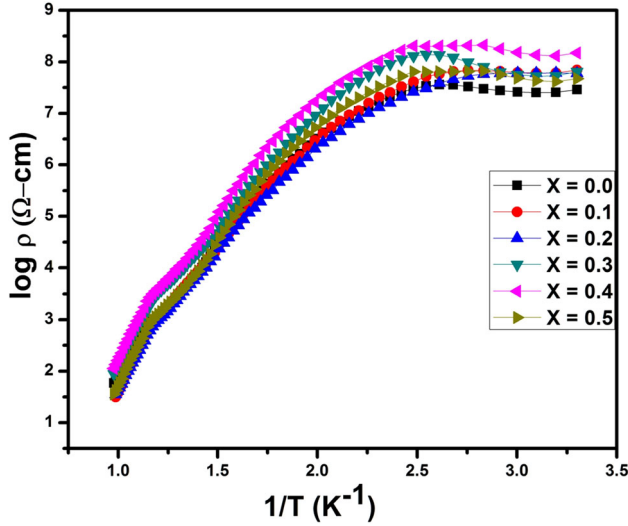Fig. 4. Variation of DC resistivity as a function of temperature for $Ni_{1-x}Mg_xFe_2O_4$ ferrites.

Fig. 5. Variation of drift mobility with temperature for $Ni_{1-x}Mg_xFe_2O_4$ ferrites.

of electrons between the ions of the same elements is present in more than one valence state and randomly distributed over crystallographic equivalent lattice sites.[20] In addition, hopping of holes between Ni^{2+} and Ni^{3+} on B-sites will contribute to electric conduction in ferrites. The conduction mechanism of holes depends on the magnesium concentration at the expense of nickel. The decrease in DC resistivity may be attributed to the changes in the distribution of cations in ferrites as well as the difference in ionic size of the cations.

The electrons are localized in ferrites, and there is a small overlap between the wave functions of ions situated on adjacent sites. Under lattice vibrations, the metal ions occasionally come closer and closer because of the transfer of electrons from one ion to another that occurs with high probability.[21] The activation energy of ferrites is calculated by plotting the graph of DC resistivity (ρ) with respect to temperature using the Arrhenius relation,

$$\rho = \rho_0 \times \exp\left(\frac{\Delta E}{K_B T}\right) \quad (3)$$

where ρ_0 is a temperature independent constant, ΔE—activation energy, K_B—Boltzmann constant, and T—absolute temperature.

Figure 4 shows that at a particular temperature the change in slope occurs in all the ferrite samples. The change in slope is nothing but the Curie temperature, and this is because of the transition of phase from ferromagnetic to paramagnetic. The activation energy of the paramagnetic phase (ΔE_1) and the ferromagnetic phase (ΔE_2) are estimated through the slopes of the curve before and after transition of phase using the following relation,
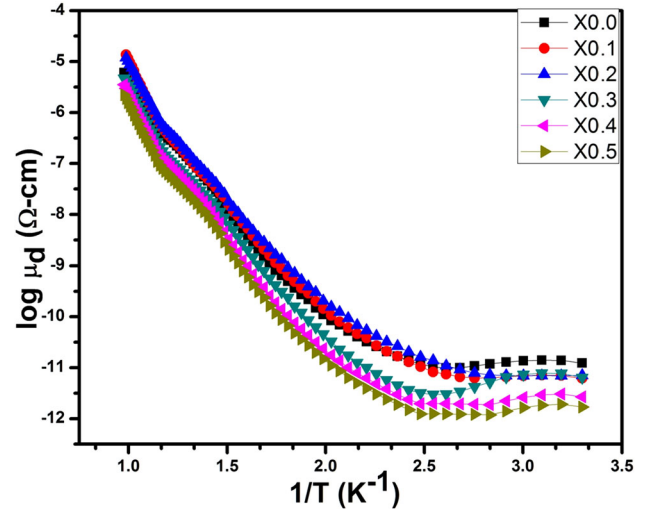
$$E = 1.98 \times 10^{-4} \times slope \ eV \quad (4)$$

The estimated values of activation energy of all the ferrite samples are tabulated in Table I. The obtained values of activation energy (ΔE_1) for the paramagnetic region ranges from 0.716 eV to 0.854 eV and the activation energy (ΔE_2) for the ferromagnetic region ranges from 1.33 eV to 2.96 eV. The estimated values of activation energy are in good agreement with each other for other spinel ferrites.[22–24] From the Table I, it is clear that the activation energy in the paramagnetic region is higher than that in the ferromagnetic region, and this is in good agreement with the theory of Irkin and Turor.[41] The lowering of activation energy in the ferromagnetic region is attributed to the spin disordering effect. However, the activation energy observed for all the ferrite samples (> 0.2 eV) indicates the small polaron hopping type of conduction mechanism. Figure 5 shows the temperature dependence of drift mobility (μ_d). The increase in drift mobility with increase in temperature may be due to the fact that charge carriers overcome the activation energy barrier resulting in increase in their mobility by getting additional energy due to the increase of temperature. Drift mobility increases with increase in temperature for all the samples resulting in the hopping of electron charge carriers from one site to another site.[25]

Frequency Dependent Dielectric Properties

The variations of dielectric constant with frequency for all ferrite samples are as shown in Fig. 6. The dielectric constant with frequency results due to heterogeneous structure of the ferrites. Initially at the low frequency region, the dielectric constant decreases rapidly, and in the high frequency region, it remains constant. This behavior shows the usual dielectric dispersion behavior as explained based on
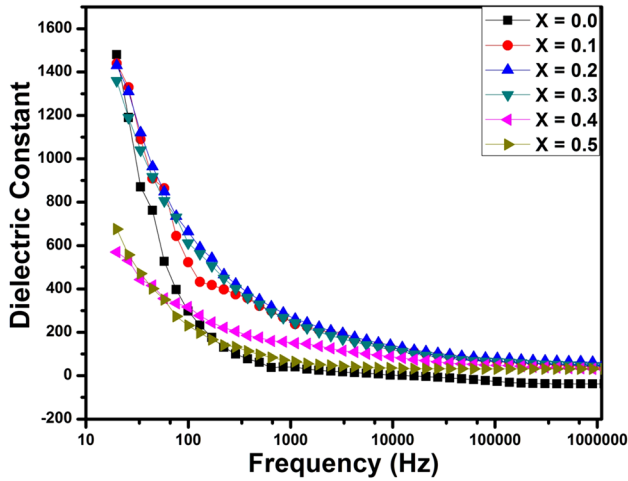
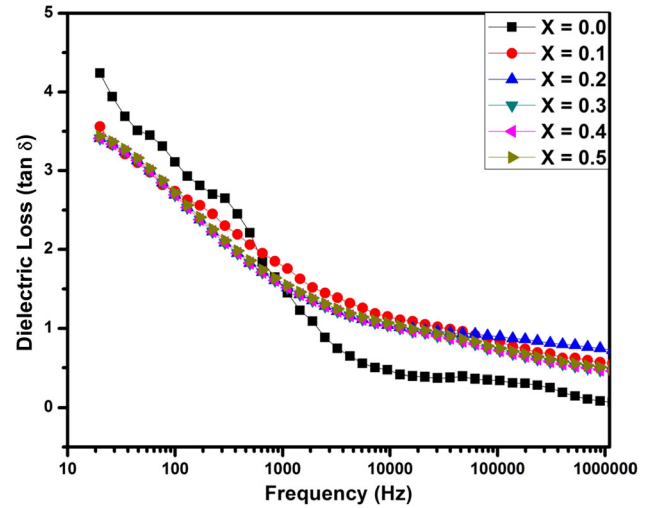Fig. 6. Variation of dielectric constant with frequency for $Ni_{1-x}Mg_{x}$-Fe_2O_4 ferrites.

Fig. 7. Variation of dielectric loss with frequency for $Ni_{1-x}Mg_xFe_2O_4$ ferrites.

the Maxwell–Wagner type interfacial polarization, which is in good agreement with Koop's phenomenological theory.[11,26] The dielectric polarizations in ferrites were similar to that of the hopping of electrons in the conduction mechanism. The dielectric constant with the frequency of all ferrite samples was estimated using the expression as follows,

$$\varepsilon' = \frac{C_p \times t}{\varepsilon_0 A} \qquad (5)$$

where ε'—dielectric constant, C_p—parallel capacitance, t—thickness of the pellets, ε_0—permittivity of free space, and A—area of the sample.

In general, the dielectric constant as a function of frequency contributed by the atomic and electronic polarizations in ferrite grains. The dielectric constant (ε') of the ferrites decreases with increase in frequency due to the hopping of electrons between $Fe^{2+} \leftrightarrow Fe^{3+}$ ions; however, the dielectric constant fails to follow the applied alternating electric field beyond a certain frequency.[27] The presence of Mg^{2+} ions gives rise to p-type charge carriers in addition to the n-type charge carriers that may be arising due to the electron exchange between Fe^{2+} and Fe^{3+} ions. The anomalous dielectric behavior is explained due to a collective contribution of n-type and p-type charge carriers to the polarization mechanism.[28] The dielectric loss tangent ($\tan\delta$) as a function of frequency at room temperature is studied, and the graph is as shown in Fig. 7. The dielectric loss tangent shows a decreasing trend with increase in frequency for all the ferrite samples as the same as that of the dielectric constant. The dielectric loss tangent is high at low frequency and drops rapidly at higher frequency; this is explained by Iwauchi,[29] and there is a strong correlation between dielectric behavior and the conduction mechanism in ferrite.
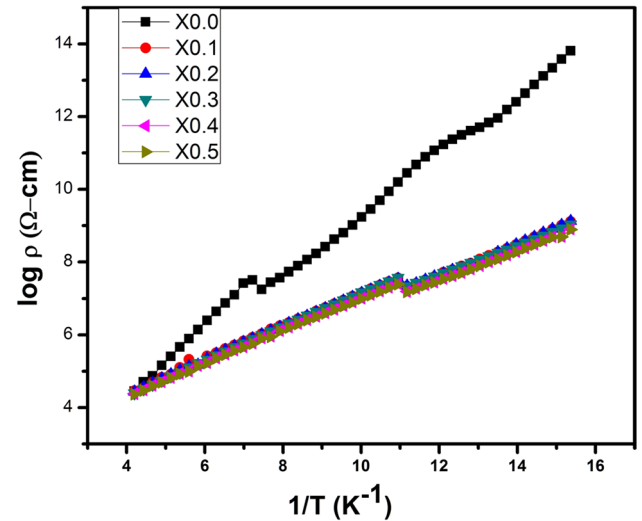

Fig. 8. AC conductivity with respect to frequency at room temperature for $Ni_{1-x}Mg_xFe_2O_4$ ferrites.

AC Conductivity Measurement

Figure 8 shows the frequency dependence of AC conductivity at room temperature for the various Mg^{2+} content in the ferrites. From Fig. 8, it is clear that all the samples show a linear AC conductivity with increase in frequency, which is a general behaviour of ferrites. The variation of AC conductivity with frequency explains the behavior of the thermally activated conduction mechanism and the type of polaron hopping responsible for conduction of electrons in the ferrite system. The AC conductivity can be determined by using the values of dielectric constant and dielectric loss factor with the relation as follows,

$$\sigma_{AC} = \varepsilon' \varepsilon_0 \omega \tan \delta \qquad (6)$$

where ε' is the dielectric constant, ε_0 is the permittivity of free space, ω is the frequency of the applied field, and $\tan\delta$ is the dielectric tangent loss.

There are two types of polaron hopping mechanisms in ferrites, namely, small polarons and large polarons. The increase of conductivity with increase in frequency was due to the small polaron model, whereas decrease of conductivity with increase in frequency was due to the large polaron hopping model,[30] the polaron hopping type of conduction mechanism was explained in detail by Austin Mott and Appel.[31] Alder and Feinleib also explained that the direct frequency-dependent conduction mechanism is due to the small polaron hopping type of conduction electrons in ferrite.[32] Figure 8 clearly shows that the AC conductivity increases with increase in frequency indicating that the small polaron hopping type of conduction electrons. However, a slight decrease in the conductivity at a particular frequency is due to the mixed polaron (small/large) hopping type of conduction.[33]

The conduction mechanism process in Mg-substituted nickel ferrites takes place through the exchange of electrons between Fe^{2+} and Fe^{3+} cations at the octahedral site. The increase in AC conductivity does not mean that the number of charge carriers increases, but only the rate of hopping of charge between the charge carriers Fe^{2+} and Fe^{3+} increases. The rate of hopping is enhanced once the

frequency of the applied field increases, resulting in increase of AC conductivity and decrease of resistivity. In the electron hopping model, it is possible to distinguish different characteristic regions at low frequencies where the AC conductivity is constant; the mechanism of transport of charge carriers takes place via many paths. The electron hopping mechanism becomes the sole contribution to the AC conductivity process in the frequency region. At sufficiently high frequencies, the resistivity remains constant due to the fact that rate of hopping of charge carriers does not follow the applied electric field in the higher frequency region, this leads to the saturation point.

Elastic Properties

The elastic behavior of ferrite materials was studied using FTIR spectrographs. The other structural parameters such as ionic radii of A and B-sites (r_A and r_B), theoretical lattice constant (a_t), oxygen positional parameter (u), tetrahedral bond length (d_{AL}), octahedral bond length (d_{BL}), tetrahedral edge length (d_{AE}), octahedral edge length (d_{BE}), unshared octahedral edge length (d_{BEU}), jump lengths of A and B-sites (L_A and L_B) were estimated from the FTIR spectrograph[26] and are tabulated in Table II. The elastic parameters such as bulk modulus (B), modulus of rigidity (G), Young's modulus (E), Poisson's ratio (σ), longitudinal elastic wave velocity (V_1), transverse elastic wave velocity

Table II. Structural and elastic parameters of Mg-substituted nickel ferrites

Parameters	X = 0.0	X = 0.1	X = 0.2	X = 0.3	X = 0.4	X = 0.5
a_0 (Å)	8.3353	8.3440	8.3306	8.3471	8.3472	8.3485
a_t (Å)	7.8855	7.8892	7.893	7.8967	7.9005	7.9056
$\rho \times 10^3$(kg/m^3)	5.3739	5.278	5.225	5.115	5.0368	4.9645
r_A (Å)	0.645	0.6525	0.66	0.6675	0.675	0.6851
r_B (Å)	1.335	1.3305	1.326	1.3215	1.317	1.306
u	0.3917	0.392	0.3927	0.393	0.3935	0.3941
d_{AL}	2.0456	2.05	2.0601	2.0644	2.0716	2.0805
d_{BL}	1.9518	1.9515	1.943	1.9468	1.945	1.9394
d_{AE}	3.3406	3.3512	3.3623	3.376	3.388	3.3948
d_{BE}	2.5532	2.5488	2.5282	2.5261	2.5143	2.5001
d_{BEU}	2.9599	2.963	2.9594	2.9664	2.9668	2.9678
L_A	3.6091	3.613	3.607	3.614	3.6143	3.6215
L_B	2.9465	2.9496	2.9448	2.9506	2.9507	2.9523
$v_1 \times 10^2$ (m^{-1})	415	420	422	424	426	427
$v_2 \times 10^2$ (m^{-1})	607	609	609	609	604	603
K_t (N/m)	1.7344	1.7752	1.7911	1.8072	1.8232	1.8365
K_0 (N/m)	3.6969	3.7217	3.7221	3.7226	3.6624	3.6631
$B \times 10^9$(kgm^{-1}s^{-2})	110.51	110.92	110.87	111.12	110.9	111.25
V_1 (m/s)	4534	4584	4606	4660	4692	4718
V_s (m/s)	2617.78	2646.65	2659.35	2690.53	2709	2856
$G \times 10^9$(kgm^{-1}s^{-2})	36.83	36.9711	36.952	37.0272	36.963	37.165
σ	0.35	0.35	0.35	0.35	0.35	0.35
$E \times 10^9$ (kgm^{-1}s^{-2})	99.4	99.82197	99.7704	99.97344	99.8001	99.9875
V_m (m/s)	2393	2419	2431	2459	2476	2487
θ (°K)	441	443.3	443.307	446.314	447.501	449.158

(V_s), mean elastic wave velocity (V_m), and Debye temperature (θ)[10] are listed in Table II.

The force constants of the tetrahedral site (k_t) and the octahedral site (k_0) were calculated employing the method suggested by Waldron.[13] According to Waldron, the force constants k_t and k_o for respective sites are given as follows,

$$K_t = 7.62 \times M_1 \times v_1^2 \times 10^{-7} \text{Nm} \tag{7}$$

$$K_0 = 10.62 \times \frac{M_2}{2} \times v_2^2 \times 10^{-7} \text{Nm} \tag{8}$$

where M_1 and M_2 are the molecular weights of cations on A- and B-sites, v_1 and v_2 are absorption bands of A and B-sites, respectively.

The bulk modulus of the ferrites in terms of stiffness constant is $B = \frac{1}{3}[C_{11} + 2C_{12}]$, where C_{11} and C_{11} are stiffness constants. According to Waldron, the isotropic materials with cubic symmetry like spinel ferrites and garnets we have C_{11}–C_{12}, i.e., $B = C_{11}$. The longitudinal elastic wave velocity (V_l) was determined using the formula suggested by Waldron, $V_l = (C_{11}/\rho)^{1/2,}$ where ρ = x-ray density, the transverse elastic wave velocity (V_s) is by general approximation $V_l = 3^{1/2}V_s$. The values of V_l and V_s were further used for the determination of elastic moduli and Debye temperature (θ) of the ferrite samples. The elastic constants were calculated using the relations[34] as follows,

$$\text{Modulus of Rigidity}(G) = \rho \times V_s^2 \tag{9}$$

$$\text{Poisson's ratio}(\sigma) = \frac{3B - 2G}{6B + 2G} \tag{10}$$

$$\text{Young's modulus}(E) = (1 + \sigma)2G \tag{11}$$

$$\text{Mean elastic wave velocity}(V_m) = \left(\frac{3V_s^3 \cdot V_1^3}{2V_s^3 + V_1^3}\right)^{1/3} \tag{12}$$

$$\text{Debye temperature}(\theta) = \frac{h}{k_B}\left[\frac{3N_A}{4\pi V_A}\right]^{1/3} \cdot V_m \tag{13}$$

where N_A is the Avogadro's number, V_A is the mean atomic volume given by $\frac{M/\rho}{q}$, where M = molecular weight, q = number of atoms (i.e. 7), and ρ = x-ray density.

From Table II, it is clear that the estimated and theoretical lattice parameters are in good agreement with each other. It confirms the estimated cation distribution of ferrites in tetrahedral and octahedral sites. The force constants of tetrahedral and octahedral sites increase with increase in Mg content.

The elastic constants such as longitudinal modulus (L), modulus of rigidity (G), bulk modulus (B),
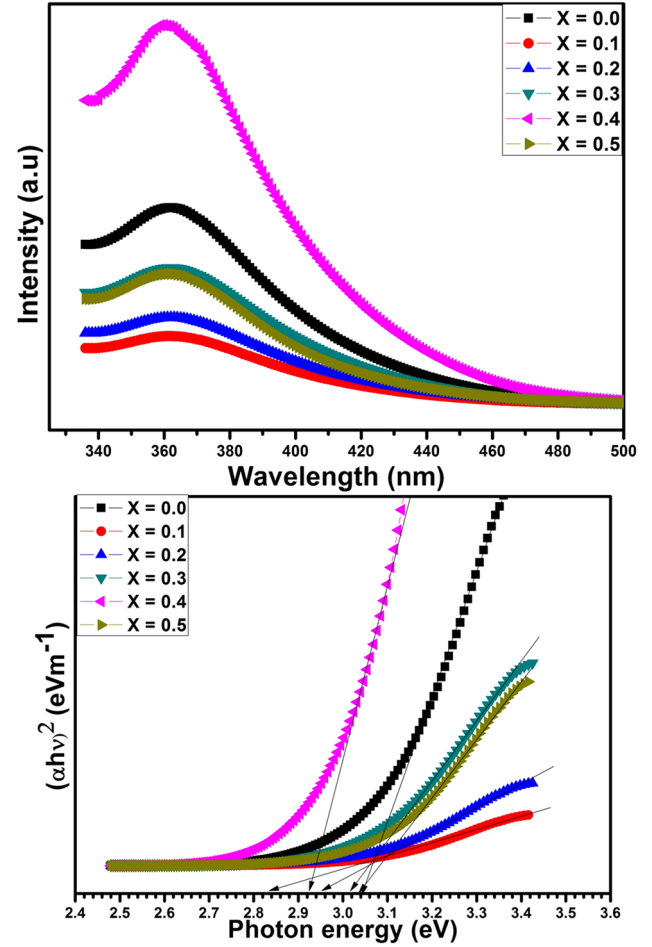

Fig. 9. UV Absorption spectrum and Tauc plot of Mg-substituted nickel ferrites at room temperature.

and Young's modulus (E) increase with increase in magnesium content, that may be due to the strengthening of interatomic bonding between various atoms continuously in ferrites. The calculated Poisson's ratio was found to be 0.35 and was constant for all the ferrites samples, which followed the isotropic elasticity nature. It is to be noted that the Debye temperature is found to increase with increase in concentration of the magnesium content.[26,34]

Optical Properties

The energy band gap of ferrite materials estimated using UV absorption spectrum and the Tauc plot is as shown in Fig. 9. Several methods are used to determine the optical properties of ferrites. The most widely used method is the Tauc model for the determination of energy gap. The optical band gap associated with the ferrites is determined through an extrapolation of the linear trend observed in the spectral dependence of $(\alpha h v)^2$ over a limited range of photon energies $h v$. The Tauc optical band gap is defined as occurring at the intercept of this linear

extrapolation with Y-axis. The absorption coefficient α near the band edge in many ferrites shows an exponential upon photon energy.[35] The direct band gap energy is derived by assuming a direct transition between the edges of the valence and the conduction band, for which the variation in the absorption coefficient with the photon energy hv is given by,

$$(\alpha h v)^2 = A\left(h v - E_g\right)^m \qquad (14)$$

where α is the absorption coefficient, A is known as the edge width parameter, E_g is the energy band gap, $m = (1/2$ and 2 for indirect and direct optical band gap) is the constant dependent on the degree of transition, where $(h v)$ is the photon energy. These direct band gap semiconductors are evaluated by plotting $(\alpha h v)^2$ versus $(h v)$ and extrapolating the tangent on the X-axis (Tauc plots). Figure 9 shows the Tauc plots for direct band gaps of the samples $Ni_{1-x}Mg_xFe_2O_4$ (with $x = 0.0$, 0.1, 0.2 and 0.3, 0.4, and 0.5), and the energy band gaps are found to be 2.99 eV, 2.25 eV, 2.48 eV, 2.84 eV, and 2.92 eV for ferrite samples, respectively (Table I).[36] We observed that the band gap energy of ferrite materials increased with increase in Mg concentration in nickel ferrites that is attributed to changes in the annealing temperatures.

The value of the direct band gap is affected by various factors such as crystallite size, structural parameters, and presence of impurities. The increase in the direct band gap for our synthesized ferrite crystals may be attributed to the greater increase in a structural parameter (lattice constant) with the increase of Mg concentration.

Magnetic Properties

The room temperature M–H hysteresis loops of magnesium-substituted nickel ferrites studied using VSM are as shown in Fig. 10. It is observed that the saturation magnetization change is due to the change of Mg^{2+} concentration in ferrites and on the method of preparation. In addition, the magnetic properties are dependent on the morphology of the grains and the microstructure of the final products. The parameters such as saturation magnetization (M_s), magnetic moment (μ_B), magnetization per gram of the samples (σ_s') and remnant magnetization (M_r), decreases with increase in Mg ion content in the ferrites, whereas the ratio of M_r/M_s are found to be increased and are tabulated in Table III. The saturation magnetization in emu/gm for a given porosity of the sample is estimated by using relation,

$$M_s = (1 - p)d_x\sigma_s'\text{emu/gm} \qquad (15)$$

where $p =$ Porosity $= \frac{(d_x - d_a)}{d_x} \times 100$, $d_x =$ x-ray density, and $d_a =$ actual density.

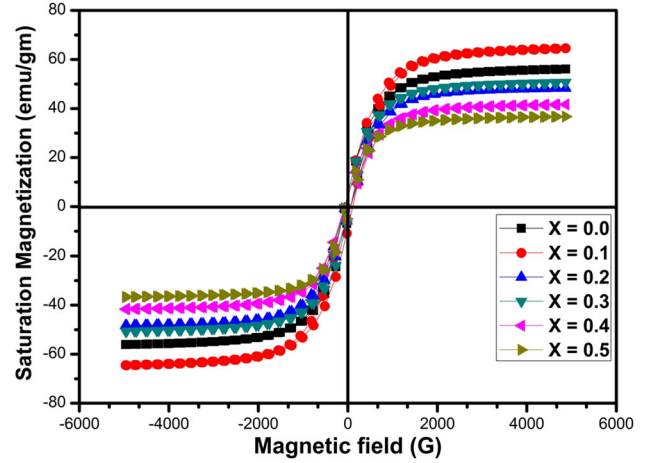The magnetic moment in the Bohr magnetron was estimated by using the relation,

Fig. 10. M–H hysteresis loops of Mg-substituted nickel ferrites at room temperature.

$$\mu = \left[\frac{M_{\text{mole}}}{5585}\right] \times \sigma_s' \qquad (16)$$

$$\sigma_s' = \frac{\mu}{M_{\text{mole}}} \times 5585 \qquad (17)$$

where M_{mole} is the molecular weight of the samples, and σ_s' is the magnetization per gram of the samples.

The decrease of saturation magnetization and magnetic moment with increase in Mg content is attributed to the surface spin effect and cation distribution on A-sites and B-sites. The decrease in these values results from the existence of spin canting effects already reported in several ferrites that are attributed to surface structure disorder.[37] Thus, the energy of a magnetic particle in the external field is proportional to its size via the number of magnetic particles in a single magnetic domain. The addition of Mg^{2+} divalent metal ion content in ferrites reduces the amount of Ni^{2+} ions and increases the amount of Fe^{3+} ions on B-sites and is responsible for the decrease of saturation magnetization and magnetic moment, which obey Nell's two-sublattice model. It is due to the energy of magnetic particles in the external magnetic field as being directly proportional to its grain size via the number of magnetic particles in single domain magnetic materials. When this energy becomes comparable to thermal energy, thermal fluctuations significantly reduce the total magnetic moment of the ferrite sample at a given field because of the large surface to volume ratio of the particles. As long as there is no external magnetic field applied, a time-averaged net magnetic moment of ferrites measures as zero. This situation is called as superparamagnetic state of a ferrite system.

The ratio of M_r/M_s increases up to 0.092368 for $X = 0.5$ which indicates the fraction of the particles in the blocked state.[38] However, the small values of

Table III. Saturation magnetization (M_s), magnetic moment (μ_B), magnetization per gram of the samples (σ_s'), and remnant magnetization (M_r), coercivity and ratio of M_r/M_s

X content	M_s (emu/gm)	μ_B	σ_s'	Remnant magnetization (M_r)	Coercivity (H_c)	M_r/M_s
0.0	64.54	2.71	13.5	4.48	0.022	0.069
0.1	56.12	2.32	11.9	4.33	0.014	0.077
0.2	50.68	2.03	10.9	3.59	0.013	0.068
0.3	48.28	1.97	10.4	3.59	0.015	0.071
0.4	41.63	1.64	9.15	3.31	0.006	0.086
0.5	36.69	1.43	9.03	3.32	0.005	0.092

M_r/M_s are due to the existence of multidomain (MD) particles in all the ferrite samples. The saturation magnetization is primarily determined by anisotropy and the A–B exchange of interaction between them.[39] On the contrary, M_s shows a decreasing trend with increasing Mg content that can be attributed to the increased migration of Fe^{3+} ions from the A- to B-sites with increasing Mg content in order to accommodate the increased number of Mg ions on A-sites as per their site preference. This migration results in an increase in Fe^{3+} content on B-sites, which gives rise to antiparallel spin coupling and spin canting resulting in weakening the A–B exchange interaction reducing thereby the saturation magnetization. However, the exchange interaction depends on cation distribution. The cation–cation distances are generally large in ferrites; therefore, direct interactions are negligible. According to Nell's theory of ferrimagnetism, there are three types of exchange interaction taking place between unpaired electrons of cations located in A and B sublattices. These are designated as,

1. Tetrahedral–tetrahedral interaction,
2. Tetrahedral–octahedral interaction,
3. Octahedral–octahedral interaction.

The exchange interaction in cubic spinel ferrites correspond to an anti-parallel alignment of magnetic moments of A-sites and B-sites; such interaction is mediated by the oxygen ions in a super exchange interaction.[40] Although all types of interactions between the 3d transition-metal ions in spinel ferrites are antiferromagnetic, those between the ions situated in the tetrahedral sites and octahedral sites are the strongest ones. If the tetrahedral sites are sufficiently populated by the magnetic ions, the ions of octahedral sites will have their magnetic moment in the opposite direction than the moments of ions from tetrahedral sites.

CONCLUSIONS

The polycrystalline ferrite materials were successfully synthesized by the solid state reaction method for the structural, optical, electrical, dielectric, and magnetic properties studies. The crystallite size calculated from the Debye–Scherer formula was found to vary from 0.963 μm to 1.069 μm and was in good agreement with AFM measurement. The FTIR absorption bands of the tetrahedral and octahedral sites were found to be around 420 cm^{-1} and 609 cm^{-1} that confirmed the formation of single phase cubic structural of ferrites. We observed that DC resistivity decreases with increasing temperature that might be due to the increase in drift mobility of the charge carriers in the ferrites, it shows the semiconductor nature of ferrite. The linear variations of AC conductivity with frequency confirm the small polaron hopping type of conduction mechanism present in ferrite samples. The elastic parameters, i.e., longitudinal modulus, rigidity modulus, bulk modulus, and Young's modulus are found to increase with increase in the magnesium content, which may be explained in terms of interatomic bonding between various atoms as strengthened continuously. The saturation magnetization and magnetic moments are found to decrease with increase of magnesium content in ferrite. The exchange interaction in spinel ferrites corresponds to anti-parallel alignment of magnetic moments of A-sites and B-sites obeying Nell's two-sublattice model. The small value of M_r/M_s indicates the existence of multidomain (MD) particles in the ferrite samples.

ACKNOWLEDGEMENT

REFERENCES

1. Q.A. Pankhurst, J. Connolly, S.K. Jones, and J. Dobson, *J. Phys. D Appl. Phys.* 36, 167 (2003).
2. J. Kulikowski, *J. Magn. Magn. Mater.* 41, 56 (1990).
3. M.A. El Hiti, *J. Phys. D Appl. Phys.* 29, 501 (1999).
4. A. Largeteau, J.M. Reau, and J. Raves, *Phys. Stat. Sol. (a)* 111, 627 (1990).
5. A.M. Abdeen, *J. Magn. Magn. Mater.* 192, 121 (1999).
6. C.G. Koops, *Phys. Rev.* 83, 121 (1951).
7. F. Haberey and H. Wijn, *Phys. Stat. Sol. (a)* 26, 231 (1968).
8. V.R.K. Murthy and J. Sobhanadri, *Phys. Stat. Sol. (a)* 3, 647 (1976).

9. M. Naeem, N.A. Shah, I.H. Gul, and A. Maqsood, *J. Alloys Compd.* 487, 739 (2009).
10. M.A. Gabal and Y.M. Al Angari, *Mater. Chem. Phys.* 118, 153 (2009).
11. P.B. Belavi, G.N. Chavan, L.R. Naik, R. Somashekar, and R.K. Kotnala, *Mater. Chem. Phys.* 132, 138 (2012).
12. T.J. Shinde, A.B. Gadkari, and P.N. Vasambekar, *Mater. Chem. Phys.* 111, 87 (2008).
13. R.D. Waldron, *Phys. Rev.* 99, 1727 (1955).
14. V.A.M. Brabers, *Phys. Status Sol.* 33, 563 (1969).
15. P.P. Hankare, V.T. Vader, N.M. Patil, S.D. Jadhav, U.B. Sankpal, M.R. Kadam, B.K. Chougule, and N.S. Gajbhiye, *Mater. Chem. Phys.* 113, 233 (2009).
16. N.M. Mahmoodi, *J. Taiwan Inst. Chem. Eng.* 44, 322 (2013).
17. R.S. Gaikwad, S.-Y. Chae, R.S. Mane, S.-H. Han, O.-S. Joo, SAGE-Hindawi Access to Res. *Int. J. Electrochem.* 2011, 1 (2011).
18. R.S. Devan, B.K. Chougule, and Y.D. Kolekar, *J. Phys.: Condens. Matter* 18, 9809 (2006).
19. E.J.W. Verwey, F. de Boer, and J.H. van Santen, *J. Chem. Phys.* 16, 1091 (1948).
20. G.N. Chavan, P.B. Belavi, L.R. Naik, B.K. Bammannavar, K.P. Ramesh, and S. Kumar, *Int. J. Sci. Technol. Res.* 2, 82 (2013).
21. R.C. Kambale, P.A. Shaikh, S.S. Kamble, and Y.D. Kolekar, *J. Alloys Compd.* 478, 599 (2009).
22. A.M. El-Sayed, *Mater. Chem. Phys.* 82, 583 (2003).
23. M.U. Islam, T. Abbas, S.B. Niazi, Z. Ahmad, S. Sabeen, and M.A. Chaudhry, *Solid State Commun.* 130, 353 (2004).
24. G.M. Kale and T. Asokan, *Appl. Phys. Lett.* 62, 2324 (1993).
25. N. Rezlescuu and E. Cuciureanu, *J. Phys. Chem. Solids* 32, 1096 (1971).
26. P. Chavan and L.R. Naik, *Int. J. Eng. Sci. Res.* 6, 29 (2016).
27. R.F.G. Gardner, R.L. Moss, and D.W. Tanner, *Br. J. Appl. Phys.* 17, 55 (2002).
28. N. Sivakumar, A. Narayanasamy, J.M. Greneche, R. Murugaraj, and Y.S. Lee, *J. Alloys Compd.* 504, 395 (2010).
29. K. Iwauchi, *Jpn. J. Appl. Phys.* 10, 1520 (1971).
30. D.R. Patil and B.K. Chougule, *J. Alloys Compd.* 458, 335 (2008).
31. H.H. Qiu, M. Kudo, and H. Sakata, *Mater. Chem. Phys.* 51, 233 (1997).
32. D. Adler and J. Feinleib, *Phys. Rev. B* 2, 3112 (1970).
33. S.L. Kadam, K.K. Patankar, C.M. Kanamadi, and B.K. Chougule, *Mater. Res. Bull.* 39, 2265 (2004).
34. K.B. Modi, M.K. Rangolia, M.C. Chhantbar, and H.H. Joshi, *J. Mater. Sci.* 41, 7308 (2006).
35. L. Said Jan and M. Ahmed Siddig, *Chin. J. Polym. Sci.* 29, 181 (2011).
36. A.I. Ahmed, M.A. Siddig, A.A. Mirghni, M.I. Omer, and A.A. Elbadawi, *Adv. Nanopart.* 4, 45 (2015).
37. A.E. Berkowitz, W.J. Schuele, and P.J. Flanders, *J. Appl. Phys.* 39, 1261 (1968).
38. A.B. Gadkari, T.J. Shinde, and P.N. Vasambekar, *J. Mater. Sci.: Mater. Electron.* 21, 96 (2010).
39. A. Verma and R. Chatterjee, *J. Magn. Magn. Mater.* 306, 313 (2006).
40. M. Siva Ram Prasad, B.B.V.S.V. Prasad, B. Rajesh, K.H. Rao, and K.V. Ramesh, *J. Magn. Magn. Mater.* 323, 2115 (2011).
41. Y.P. Irkin and E.A. Turor, *Sovt. Phys. JEPT.* 33, 673 (1957).